



HAL
open science

Low-mode internal tides and balanced dynamics disentanglement in altimetric observations: Synergy with surface density observations

Aurélien L. Ponte, Patrice Klein, Michael Dunphy, Sylvie Le Gentil

► **To cite this version:**

Aurélien L. Ponte, Patrice Klein, Michael Dunphy, Sylvie Le Gentil. Low-mode internal tides and balanced dynamics disentanglement in altimetric observations: Synergy with surface density observations. *Journal of Geophysical Research. Oceans*, 2017, 122, pp.2143-2155. 10.1002/2016JC012214 . insu-03682751

HAL Id: insu-03682751

<https://insu.hal.science/insu-03682751>

Submitted on 1 Jun 2022

HAL is a multi-disciplinary open access archive for the deposit and dissemination of scientific research documents, whether they are published or not. The documents may come from teaching and research institutions in France or abroad, or from public or private research centers.

L'archive ouverte pluridisciplinaire **HAL**, est destinée au dépôt et à la diffusion de documents scientifiques de niveau recherche, publiés ou non, émanant des établissements d'enseignement et de recherche français ou étrangers, des laboratoires publics ou privés.

Copyright

RESEARCH ARTICLE

10.1002/2016JC012214

Key Points:

- Mesoscale and submesoscale may have a signature on sea surface density
- Low-mode internal tides have a weaker signature on sea surface density
- Sea surface density may help identify low-mode internal tide signatures in altimetric data

Supporting Information:

- Supporting Information S1
- Figure S1

Correspondence to:

A. L. Ponte,
aurelien.ponte@ifremer.fr

Citation:

Ponte, A. L., P. Klein, M. Dunphy, and S. Le Gentil (2017), Low-mode internal tides and balanced dynamics disentangle in altimetric observations: Synergy with surface density observations, *J. Geophys. Res. Oceans*, 122, 2143–2155, doi:10.1002/2016JC012214.

Received 5 AUG 2016

Accepted 20 FEB 2017

Accepted article online 23 FEB 2017

Published online 16 MAR 2017

Low-mode internal tides and balanced dynamics disentangle in altimetric observations: Synergy with surface density observations

Aurélien L. Ponte¹ , Patrice Klein¹, Michael Dunphy¹ , and Sylvie Le Gentil¹

¹Univ. Brest, CNRS, IRD, Ifremer, Laboratoire d'Océanographie Physique et Spatiale (LOPS), IUEM, Brest, France

Abstract The performance of a tentative method that disentangles the contributions of a low-mode internal tide on sea level from that of the balanced mesoscale eddies is examined using an idealized high resolution numerical simulation. This disentanglement is essential for proper estimation from sea level of the ocean circulation related to balanced motions. The method relies on an independent observation of the sea surface water density whose variations are 1/ dominated by the balanced dynamics and 2/ correlate with variations of potential vorticity at depth for the chosen regime of surface-intensified turbulence. The surface density therefore leads via potential vorticity inversion to an estimate of the balanced contribution to sea level fluctuations. The difference between instantaneous sea level (presumably observed with altimetry) and the balanced estimate compares moderately well with the contribution from the low-mode tide. Application to realistic configurations remains to be tested. These results aim at motivating further developments of reconstruction methods of the ocean dynamics based on potential vorticity dynamics arguments. In that context, they are particularly relevant for the upcoming wide-swath high resolution altimetric missions (SWOT).

1. Introduction

Two decades ago, the advent of radar nadir altimetry has provided oceanographers with global knowledge of large-scale sea surface height (SSH) at scales longer than 200 km and enabled a giant stride forward in our understanding of the turbulent nature of the oceanic circulation associated with mesoscale eddies [Le Traon, 2013]. This vision of the impact of mesoscale turbulence on ocean properties was well confirmed by Ocean Global Circulation Models and climate studies [Griffies *et al.*, 2015]. SSH observations led to estimates of the near-surface ocean horizontal circulation and, once combined with Argo data, to estimates of the horizontal transport of heat and tracers [Zilberman *et al.*, 2014]. The upcoming launch of a new generation of wide-swath altimeters (SWOT, 2020) is expected to be the next stride forward: the high resolution (down to 15 km) maps of SSH that will be collected should provide access to the oceanic 3-D circulation and associated vertical transports of biochemical tracers [Fu *et al.*, 2010]. Multiple challenges lie in the development of the conceptual framework that will allow us to do so [Klein *et al.*, 2015; Arbic *et al.*, 2015].

The present work tackles one such challenge which is raised by the superposition of dynamically different signals in altimetric sea level data. Barotropic tides dominate temporal variations of sea level with typical amplitudes of order 1 m. This contribution is fortunately largely known and predictable in the open ocean with rms differences between model outputs and bottom pressure recorders below 1 cm [Stammer *et al.*, 2014].

Balanced motions, i.e., mesoscale eddies and currents with scales larger than $O(100)$ km, constitute the other dominant contribution to sea level variations with typical amplitudes of order 10 cm [Fu *et al.*, 2010]. The dynamics of these motions is strongly constrained by the Earth's rotation, which is quantitatively characterized by weak Rossby numbers (U/fL , where U and L are typical velocity and length scales, respectively, and f is the Coriolis frequency) and the ocean vertical stratification. The dynamics are said to be quasigeostrophic (QG), meaning that a diagnostic relationship called geostrophy exists between pressure and the Coriolis force ($fu = -\partial_y p / \rho_0$, $fv = \partial_x p / \rho_0$ where (u, v) is the horizontal velocity, p is the pressure, ρ_0 is a reference density). The evolution of QG motions is governed by the horizontal advection of a single 3-D variable called

potential vorticity (PV). Knowledge of PV is directly related to the geostrophic stream function ($\psi = p/\rho_0 f$) via a process called PV inversion [Hoskins *et al.*, 1985].

Internal gravity waves belong to a third dynamical class of motions that create sea level fluctuations. These waves translate fast (time periods shorter than an inertial period) propagating perturbations of the oceanic stratification. Barotropic tidal flow against bottom topography and surface winds are important sources of internal gravity waves in the ocean. Internal waves of tidal origin have a signature on altimetric observations at aliased frequencies (around 60 days for M_2 and Topex-Poseidon/Jason orbits [Dufau *et al.*, 2014]) and their amplitudes can reach up to 5 cm [Ray and Mitchum, 1996]. Such signature is extracted from altimetric data when internal tides induce sea level motions at tidal frequencies with a persistent phase relationship with respect to astronomical forcings. Internal tides are said to be “coherent” in this case, which typically occur nearby internal tide generations sites and/or in areas of weak mesoscale activity [Shriver *et al.*, 2014]. These coherent tides could therefore be taken into account BY the tidal correction of upcoming altimetric missions. Unfortunately, at least 30% of internal tide sea level variations appears to be incoherent [Zaron, 2015]. The analysis of outputs from tide resolving global numerical models of the ocean circulation suggest that, in weakly energetic areas, the contribution from fast sea level motions dominates spectra in the 15–100 km wavenumber band that will be resolved by SWOT [Richman *et al.*, 2012]. A crucial question has therefore emerged: how can we distinguish sea level motions produced by balanced flows from that produced by internal tides and more generally internal gravity waves?

This work is a first attempt at developing a method that disentangles the coexisting signatures of a turbulent baroclinic jet and a low-mode internal tide in an idealized numerical simulation. The method relies on the combination of sea level data with surface density for which sea surface temperature would be a proxy in a real case scenario. The cornerstones of the present approach are first that the signature of the low-mode internal tide on sea surface density is weak and second that sea surface density is correlated with interior potential vorticity anomalies. The invertibility principle of potential vorticity can thus be used to relate sea surface density anomalies with sea level anomalies associated with the balanced turbulence [Lapeyre and Klein, 2006]. Reasons for considering a low-mode internal tide are that they dominate the internal tide signature on sea level [Ray and Zaron, 2011] and carry most of the internal tide energy. These modes have the largest wavelengths (about 200 km for semidiurnal tides) and are already resolved with present altimeters. The propagation of low-mode internal tides is less affected by balanced turbulent eddies compared to higher modes. Their stronger coherence with respect to astronomical forcings and their resolution in existing satellite data enables the test of the method proposed here with actual data, hence the present focus on these long waves.

The numerical experiment employed to test the method is described in section 2. The entanglement of balanced and internal tide contributions to sea level and more precisely its consequences for the estimation of surface horizontal currents are presented in section 3 along with the quasigeostrophic framework. Sea surface density anomalies are described in section 4, associated tidal variations are quantified, and, the relationship between surface density anomalies and interior potential vorticity anomalies are discussed. A method is proposed in section 5 in order to distinguish balanced and internal tide contributions in sea level data. Section 6 discusses results, considers caveats, and perspectives for future work.

2. Numerical Setup

The numerical simulation analyzed here is designed to represent the propagation of a low-mode internal tide through an unstable baroclinic jet in a zonally periodic β -plane channel centered at 45°N. The numerical model is the Regional Oceanic Modeling System (ROMS) [Shchepkin and McWilliams, 2005]. The model solves the hydrostatic primitive equations in a 1024 km \times 2880 km domain with a uniform depth of 4 km. Simulations are spun up at a 4 km horizontal resolution with 50 stretched vertical levels for 1500 days, after which the grid is refined to 2 km horizontal resolution with 100 vertical levels. The vertical grid spacing ranges from 3.5 m near the surface to 200 m near the sea floor for the 2 km resolution simulation. Horizontal mixing uses a biharmonic scheme with a coefficient of 10^8 m⁴/s. Vertical diffusion in the interior uses a K-profile parameterization. Density is computed with temperature alone (salinity held constant) and a linear equation of state.

The nature of the quasigeostrophic turbulent flow that develops in the numerical simulations depends on the initial distribution of density. This initial distribution is computed by joining meridionally two density profiles $\rho_{\text{south}}(z)$ and $\rho_{\text{north}}(z)$:

$$\rho_i(x, y, z) = [1 - \gamma(y)]\rho_{\text{south}}(z) + \gamma(y)\rho_{\text{north}}(z). \quad (1)$$

The analytical details associated with these initial conditions as well as the result of stability analysis based on these are provided as supporting information text. An overview of the spun up meridional distribution of density is given in Figure 1a. Velocities are initialized to satisfy geostrophic balance. This method is similar to *Ponte and Klein [2013]* and *Ponte and Klein [2015]* except that profiles are chosen such as to have surface variations of density (see *Roulet et al. [2012]* for a discussion of the different possible regimes of turbulence). This surface meridional gradient of density leads to frontogenesis and a surface intensified turbulent activity that is visible on the vertical profile of averaged kinetic energy (Figure 1c). The meridional extent of the mesoscale turbulence is controlled with sponge layers as described in *Ponte and Klein [2015]*.

A zonally uniform mode 1 internal wave is generated in the southern part of the domain by adding a force in the meridional momentum conservation equation:

$$\mathcal{F}_v = f_0 \sin(\omega t) e^{-(y-y_{\text{wm}})^2 / \Delta_{\text{wm}}^2} \phi_1(z), \quad (2)$$

where $f_0 = 1.2 \cdot 10^{-5} \text{ m s}^{-2}$ is the amplitude of the forcing and ϕ_1 is the velocity/pressure modal structure of first baroclinic vertical mode computed with the south profile of stratification [*Gill and Clarke, 1974*]. The forcing frequency ω is 2 days^{-1} , i.e., typical of a semidiurnal tide. The forcing is centered around $y_{\text{wm}} = 400 \text{ km}$ and its meridional width Δ_{wm} is 10 km (Figure 1b). The internal wave produced is a plane wave with a wavelength of about 200 km consistent with the baroclinic mode one dispersion relation, and, a 3 cm signature on sea level (Figure 2c). The pathway of the internal wave is strongly affected by the slow balanced turbulence such as north of the turbulent jet the waves is significantly incoherent and focusing of the waves occurs as predicted by *Dunphy and Lamb [2014]*. In a companion paper, we explore dynamically the interactions between the low-mode internal tide and the balanced turbulence [*Dunphy et al., in press*]. Tidal density anomalies along a meridional section are characteristic of a mode 1 wave with a single maximum within the water column. Note that tidal density anomalies are weak at the surface, a fact that will be key to the method presented here. Relaxation layers nearby south and north boundaries absorb outgoing waves.

Throughout the manuscript, diagnostics of slow quasigeostrophic fluctuations and of internal tide fluctuations will be made based on 1 day averaging and harmonic analysis. Such diagnostics are expressed, for sea level, as:

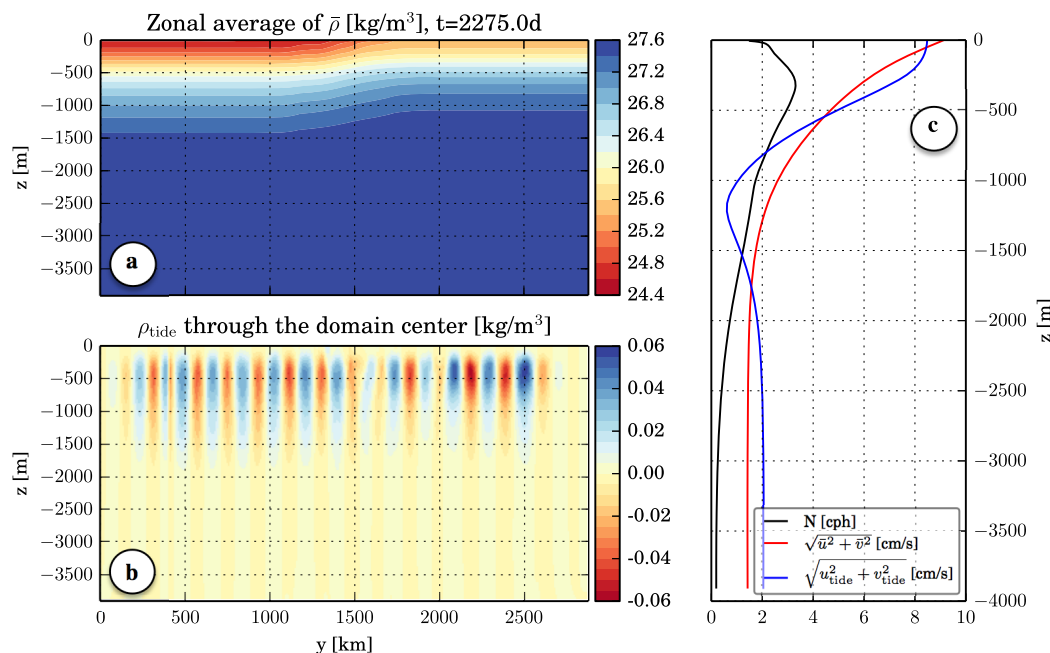


Figure 1. Meridional sections of 1 day averaged zonally (a) averaged density and (b) tidal density (estimated with a 1 day harmonic analysis). On the right (c), vertical profiles of domain averaged statistics.

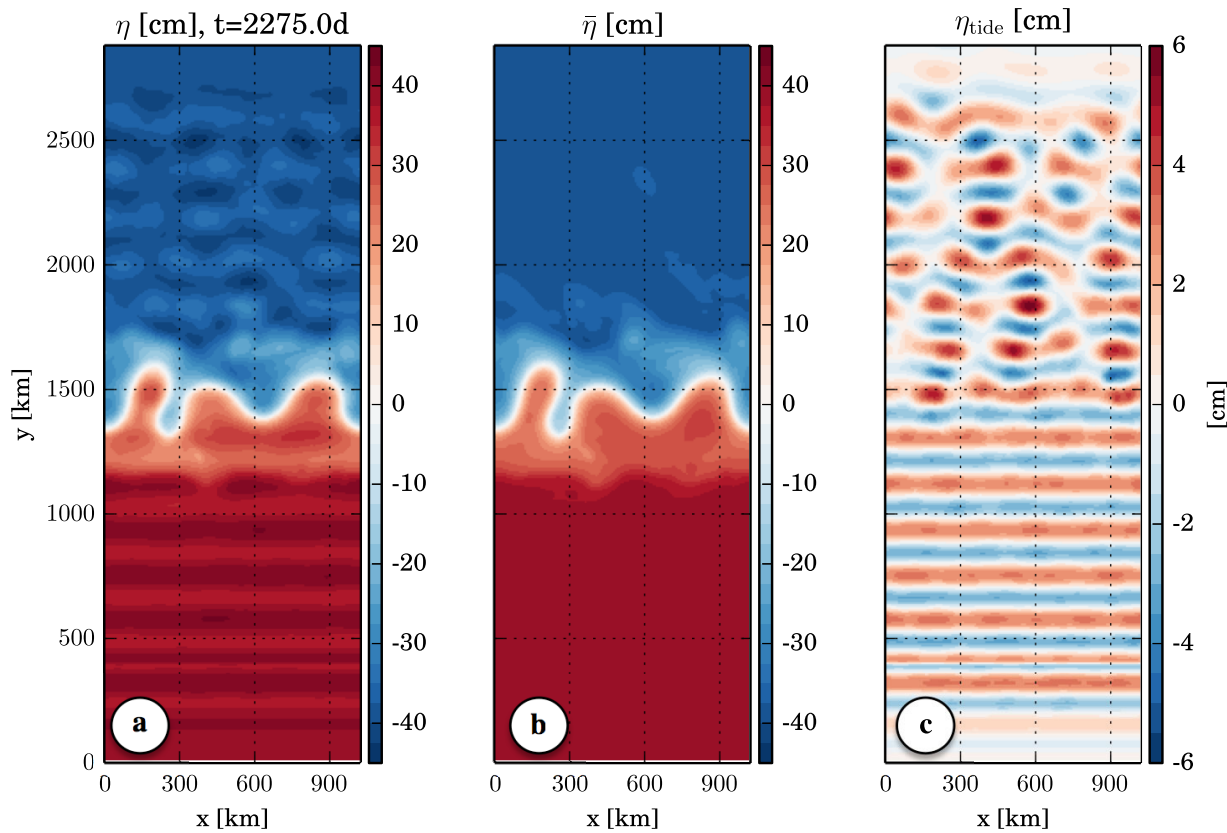


Figure 2. (a) Instantaneous, (b) 1 day averaged, and (c) tidal sea level.

$$\bar{\eta}(t) = \frac{1}{2T} \int_{t-T}^{t+T} \eta(t') dt', \quad (3)$$

$$\eta_{\text{tide}}(t) = \frac{1}{T} \int_{t-T}^{t+T} \eta(t') \times \cos \omega(t-t') dt', \quad (4)$$

where $T = 0.5$ day. These diagnostics are illustrated in Figure 2 and compared to an instantaneous values of the sea level. Note that the difference between the instantaneous sea level and the sum of $\bar{\eta}$ and η_{tide} does not exceed 1 cm and is dominated by wavy patterns with wavelengths consistent with that of a 2ω mode 1 internal wave (not shown). Instantaneous estimates of sea level or density are assumed to represent what would be obtained from satellite observations.

3. Disentanglement via PV Inversion

As a motivational example, the geostrophic zonal velocity (u_g) estimated from the instantaneous sea level is compared to the true instantaneous zonal velocity in Figures 3a and 3b. The error between estimate and truth is shown in Figure 3c. As one could have anticipated the geostrophic velocity estimates correctly the zonal velocity associated with meandering jet. The error is large outside the jet, about 40 cm/s, with a horizontal structure that is closely related to that of the internal tide (Figure 2c). The reason for such error is that the geostrophic approximation does not relate correctly tidal sea level anomalies and tidal currents. The complex amplitude of zonal current for an internal wave of frequency ω is expected to relate to tidal sea level according to:

$$\tilde{u} = \frac{-i\omega g \partial_x \tilde{\eta} + fg \partial_y \tilde{\eta}}{\omega^2 - f^2}, \quad (5)$$

where $(u, \eta) = \Re\{(\tilde{u}, \tilde{\eta})e^{-i\omega t}\}$. In comparison the geostrophic relation is given by: $u_g = -g \partial_y \eta / f$. (Note that this corresponds to (5) with $\omega = 0$.) Without an internal tide, the error magnitude would have been below

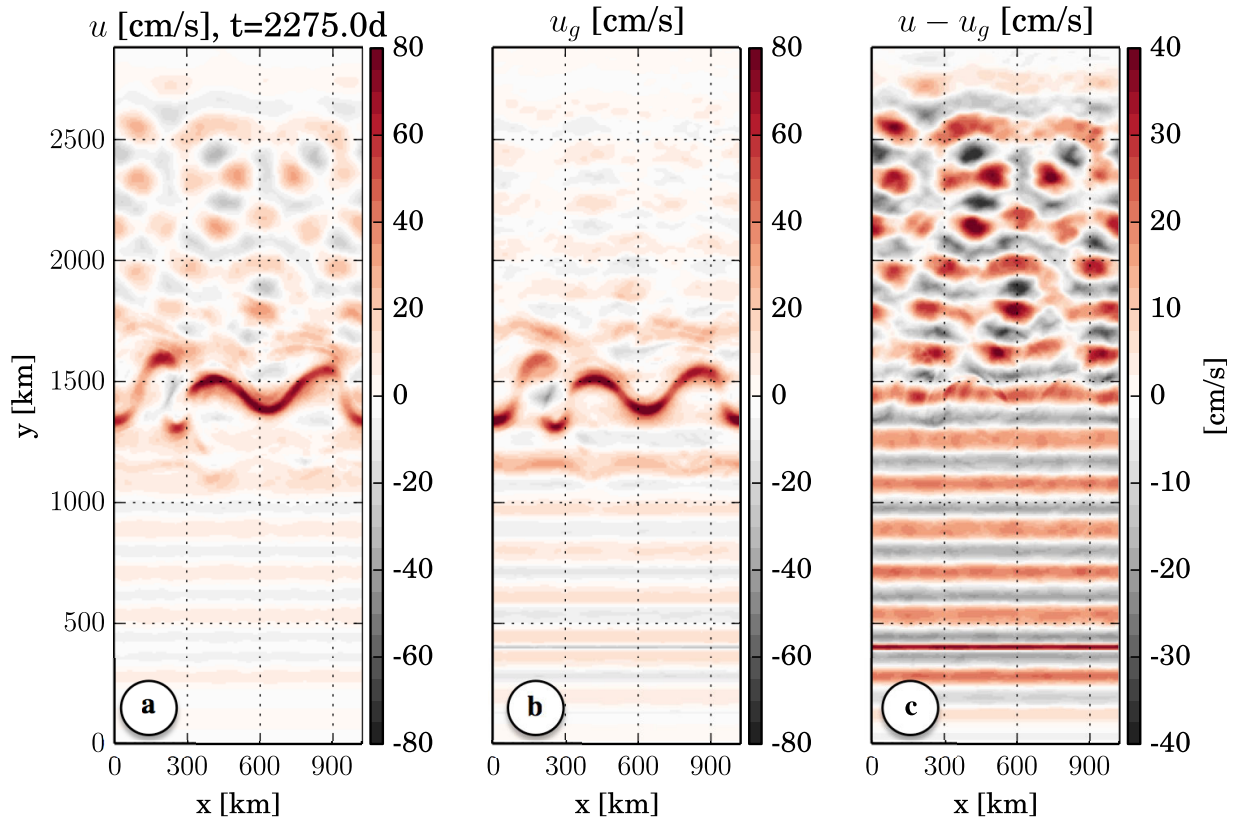


Figure 3. (a) Instantaneous zonal current, (b) geostrophic estimate, and (c) difference.

10 cm/s and confined to the northern and southern most parts of meanders (not shown) and qualitatively consistent with cyclogeostrophy [Penven *et al.*, 2014].

The question asked is whether we could distinguish contributions associated with the slower balanced turbulence from that associated with the internal tide. An underlying assumption is that the time resolution of altimeters (about 10 days) is not sufficient to discriminate both contributions with time filtering as done here. The method developed next leverages the dynamical properties of the slower balanced turbulence. The dynamics of these motions is at first-order quasigeostrophic and solely governed by the horizontal advection of the quasigeostrophic potential vorticity and top and bottom densities [Vallis, 2006]. Potential vorticity and boundary tracer anomalies describe the whole quasigeostrophic system. Potential vorticity anomalies with respect to large-scale background values is related to the geostrophic stream function ψ according to:

$$q = \nabla^2 \psi + \partial_z \left(\frac{f_0^2}{N^2} \partial_z \psi \right), \quad (6)$$

where f_0 is the value of the Coriolis frequency at the center of the domain, $N^2(z) = -g \partial_z \rho_{\text{ref}} / \rho_0$ is the Brunt-Väisälä frequency computed from the horizontal averaged density $\rho_{\text{ref}}(z)$. At the surface and bottom, density anomalies and stream function are related by the hydrostatic relation:

$$\partial_z \psi = -g \rho / \rho_0 f_0 \quad \text{for } z=0, -H. \quad (7)$$

Equation (6) subject to boundary conditions (7) represents an elliptic problem in ψ that we can solve. One day averages of the velocity and density field are used to compute an estimate of the quasigeostrophic potential vorticity according to:

$$q = \partial_y \bar{v} - \partial_x \bar{u} - \partial_z \left(\frac{g f_0 (\bar{\rho} - \rho_{\text{ref}}) / \rho_0}{N^2} \right). \quad (8)$$

Inversion of q according to boundary conditions given by 1 day averaged density anomalies leads to a stream function ψ . At the surface, this stream function is converted into an equivalent sea level $\eta_e = f_0 \psi / g$

which is shown in Figure 4a and visually compares well to the actual 1 day averaged sea level in Figure 2b. The crux of the exercise comes next when taking the difference between the instantaneous sea level and η_e . This difference (Figure 4b) resembles closely to the tidal contribution to sea level (Figure 2c). Note that using instantaneous fields for the potential vorticity inversion would have lead to a nearly identical result as internal waves have weak signature on potential vorticity. (Filtering of the internal tide via inversion of instantaneous potential vorticity turns out to be not as efficient as with temporal filtering ($\bar{\eta}$, η_{tide}) which motivates considering 1 day averaged fields. The internal tide propagation in the southern and northern parts of the domain is indeed supported by vertical profiles of stratification that differ from that used in the definition of potential vorticity which results in a weak projection of the internal tide on the balanced estimate from inversion of instantaneous fields.)

Provided estimates of the potential vorticity and top and bottom boundary conditions are available, one may thus solve the problem at hand and distinguish slow quasigeostrophic sea level from internal tide sea level in an instantaneous observation. In a real case scenario, surface temperature may provide an estimate of density for the surface boundary condition (see discussion in section 6). Bottom density anomalies are weak (see background distribution in Figure 1a). The outstanding question is whether we can make a good enough estimate of the interior potential vorticity.

4. Sea Surface Density

The cornerstone of the method consists of combining an instantaneous observation of sea level with an estimate of its balanced contribution obtained from sea surface density. The first reason motivating a combination with sea surface density is that the low-mode internal tide has a weak signature on surface density compared to the balanced turbulence (Figure 5a which shows the result of a harmonic analysis as in equation (4)). Tidal variations of sea surface density result from the horizontal advection by tidal currents of the

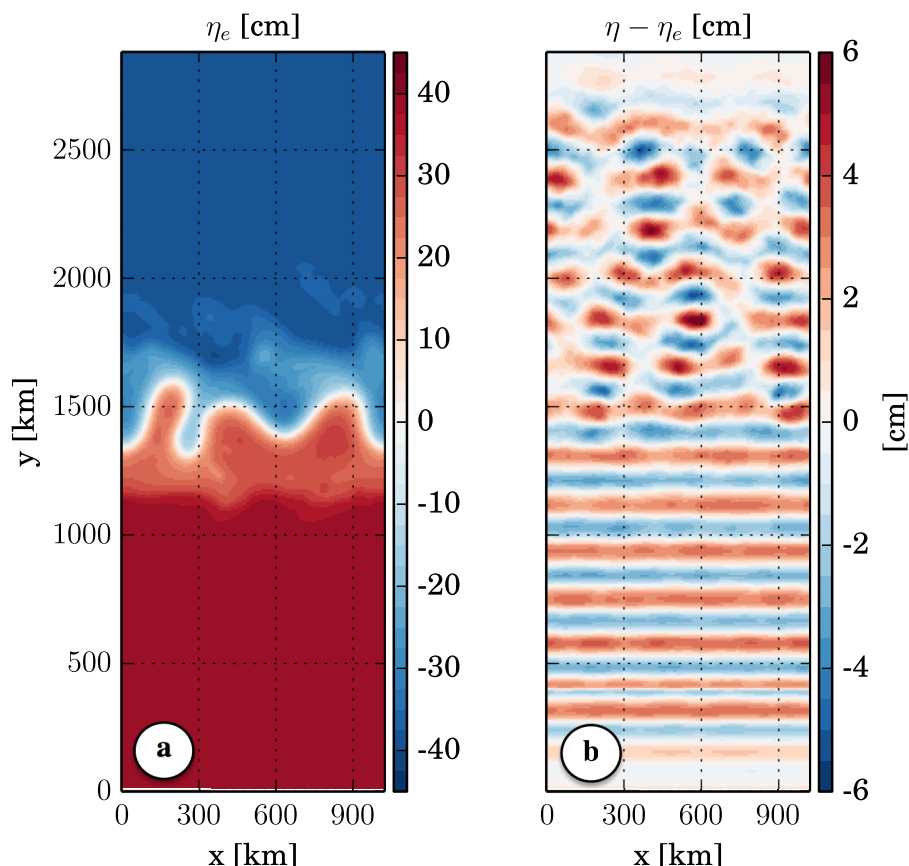


Figure 4. (a) Sea level from PV inversion and (b) difference between instantaneous sea level and that estimated from PV inversion.

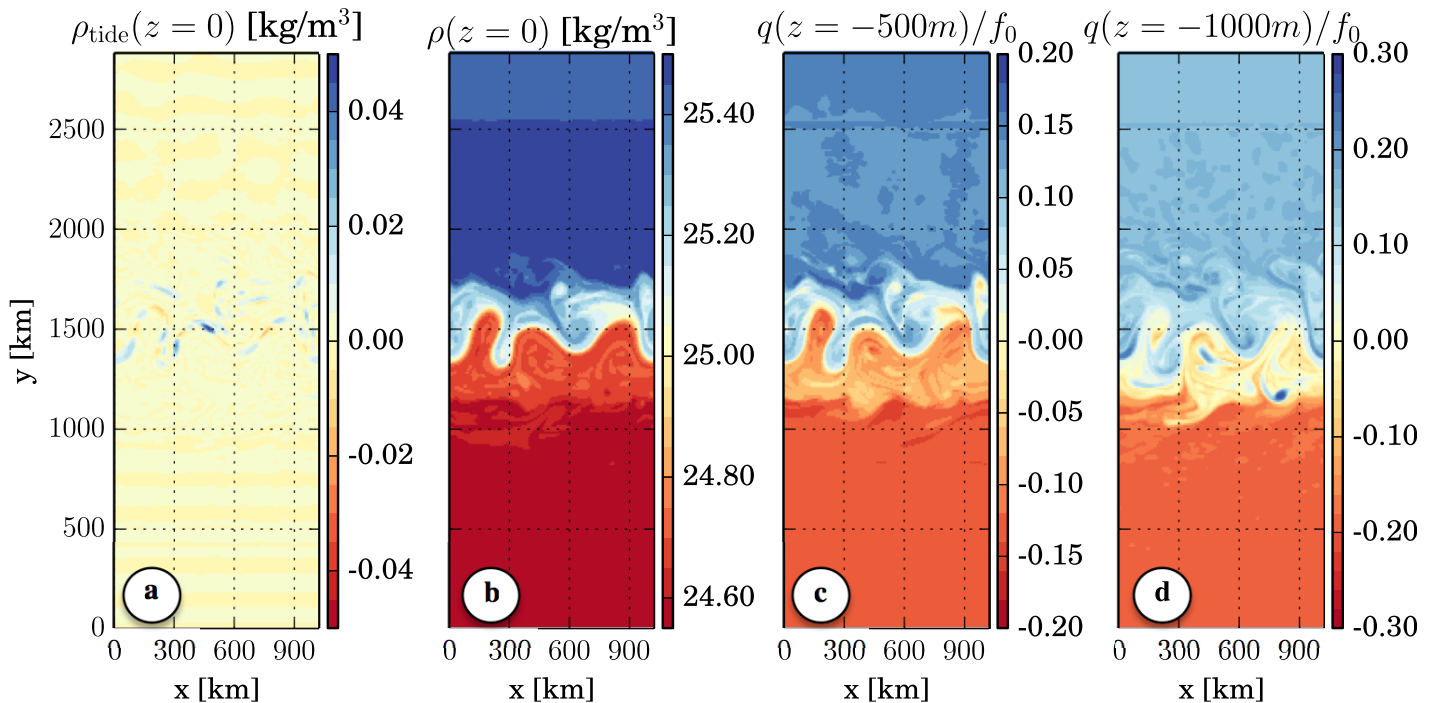


Figure 5. From left to right: (a) tidal density at the surface, (b) instantaneous density at the surface, 1 day averaged potential vorticity (c) at $z = -500$ m and (d) at $z = -1000$ m.

gradients associated with the slower balanced turbulence. These variations are largest near fronts where their amplitudes reach 0.05 kg m^{-3} . This is consistent with the product of the tidal excursion associated with the internal tide ($\lambda = u_{\text{tide}}/\omega \sim 600$ m) by balanced surface density gradients ($\nabla_h \bar{\rho} \sim 2.4 \times 10^{-5} \text{ kg/m}^4$) and an order of magnitude smaller than the sea surface density anomalies associated with the balanced turbulence. The instantaneous distribution of sea surface density (Figure 5b) is thus dominated by balanced contributions.

The second motivation behind using sea surface density in order to distinguish balanced motions from waves is that it correlates with interior potential vorticity anomalies. Comparison of instantaneous density (Figure 5b) with 1 day averaged potential vorticity maps at 500 m depth (Figure 5c) and 1000 m depth (Figure 5d) are visual evidence for this correlation. In similar numerical experiments, *Lapeyre and Klein* [2006] observed and dynamically discussed and justified the existence of such a correlation. Quantification of this relationship between surface density ρ'_s and interior PV q' anomalies is achieved with linear regressions between both variables at fixed depth. Anomalies, which are indicated by primes (\cdot'), are defined with respect to zonal means. The slope of this linear regression is:

$$\alpha(z) = \frac{\langle q' \rho'_s \rangle}{\langle \rho_s'^2 \rangle}, \quad (9)$$

where $\langle \cdot \rangle$ is a domain average. The skill of this regression is given by:

$$S(z) = 1 - \frac{\langle (q' - \alpha(z) \rho'_s)^2 \rangle}{\langle q'^2 \rangle}. \quad (10)$$

This skill is shown in Figure 6a and confirms the correlation between surface density and interior potential vorticity in the upper 1500 m of the water column. The regression coefficient $\alpha(z)$ is shown in black in Figure 6b and compared with the ratio of the large-scale potential vorticity gradient to the gradient of surface density in red:

$$\alpha_{\text{bg}}(z) = \frac{q_{\text{north}} - q_{\text{south}}}{\rho_{s,\text{north}} - \rho_{s,\text{south}}}. \quad (11)$$

North and south potential vorticity profiles are given by the vertical stretching of the density profiles that were used to define initial conditions in section 2. The good correspondence between $\alpha(z)$ and $\alpha_{\text{bg}}(z)$

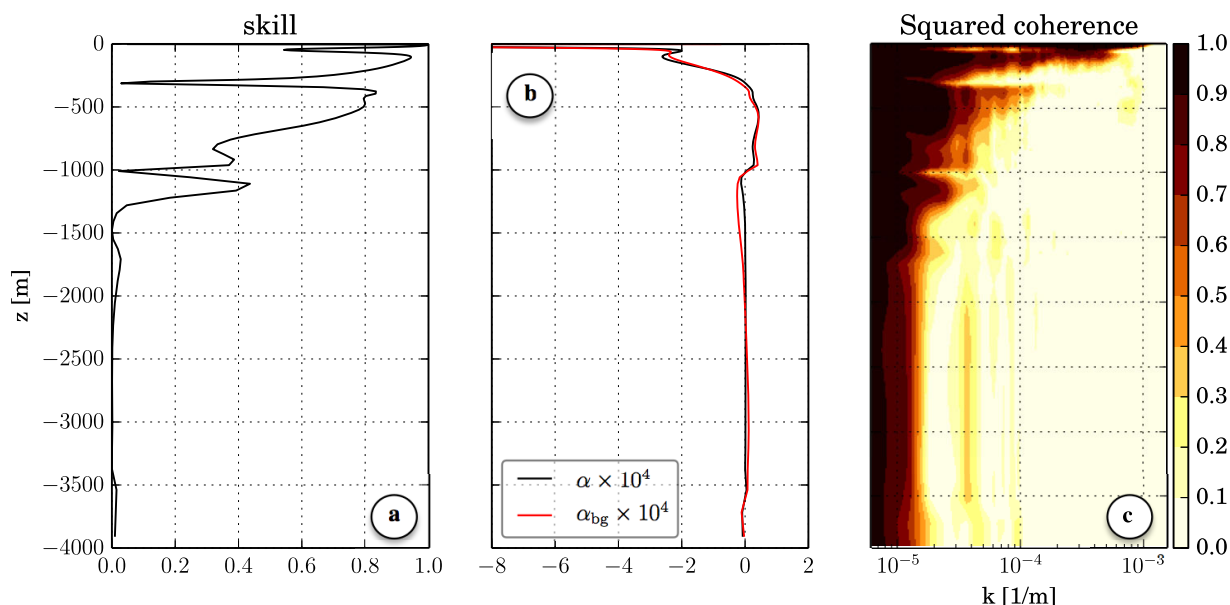


Figure 6. (a) Skill of the linear regression between surface density and PV and (b) regression coefficient alongside an estimate from the north and south profiles. (c) Squared coherence between estimate of PV and PV from surface density.

provides a means of estimating $\alpha(z)$ from the large-scale potential vorticity gradients. The latter are dominated by vortex stretching terms and could thus be derived from hydrography (Argo or climatologies). Reversals of the sign of the large-scale potential vorticity gradient coincide with local minima of the skill (350 and 1000 m water depth).

The squared coherence between the potential vorticity estimated from surface density ($q_p = \alpha \rho_s$) and the actual potential vorticity is a final diagnostic of the efficiency of this approach as a function of wavenumber and depth (Figure 6c). This squared coherence is given by:

$$C^2(k, z) = \frac{|\langle \hat{q}^* \hat{q}_p \rangle|^2}{\langle |\hat{q}|^2 \rangle \langle |\hat{q}_p|^2 \rangle}. \quad (12)$$

Larger coherences are found down to the ocean floor at lowest wave numbers. At larger wavenumbers, the coherence exhibits a maximum in surface layers, typically within the first 200 m of the water column. The signature of the reversal of large-scale potential vorticity gradient is visible on this squared coherence and impacts our ability to estimate potential vorticity from surface density.

5. Method and Results

Having shown the relationship between interior potential vorticity and surface density anomalies, sea level, and sea surface density data are now combined in order to distinguish slow balanced and internal wave signatures on sea level. The method consists first in estimating the potential vorticity q_p from surface density as described in the previous section. Inversion of this estimate of potential vorticity leads to a geostrophic stream function ψ_p that is expected to be representative of slow balanced motions. The PV inversion process is that described in section 3 except for the bottom boundary condition which is one of no flow ($\psi = 0$ at $z = -H$). A boundary condition based on density introduced spurious barotropic signals that could not be eliminated (note that such boundary condition is also imposed in Wang *et al.* [2013]). The inversion uses the instantaneous surface density for the surface boundary condition. The relative importance of the approximations performed on potential vorticity and surface and bottom boundary conditions is discussed in Appendix A. The approximated potential vorticity is the dominant source of error in the disentanglement, followed by the bottom boundary condition. The signature of internal tide on surface density does not affect this error significantly.

An overview of the equivalent sea level η_ρ obtained after PV inversion (Figure 7a) captures the meandering of the jet and the shape of 1 day averaged sea level contours (Figure 2b). Differences between $\bar{\eta}$ and η_ρ are lower than 10 cm and are localized near the meanderings (Figure 7b). The squared coherence between these two variables confirms that η_ρ correctly represents the 1 day averaged sea level across a wide range of scales (orange curve in Figure 8, bottom left). Importantly the squared coherence between $\bar{\eta}$ and η_ρ , unlike that between $\bar{\eta}$ and η (black in Figure 8, bottom left), does not exhibit a minimum around the internal tide wavelength.

The balanced contribution to sea level η_ρ is then subtracted from the instantaneous one (Figure 7c). This difference ($\eta_{\text{tide},\rho} = \eta - \eta_\rho$) is an estimate of the internal tide signature on sea level which can be compared to the result of an harmonic analysis of the sea level η_{tide} (Figure 2c) or to the difference between instantaneous and 1 day averaged sea level ($\eta - \bar{\eta}$, map not shown). In areas of low eddy kinetic energy, away from the meandering jet, $\eta_{\text{tide},\rho}$ captures correctly the tidal nature of instantaneous sea level fluctuations. Near the meandering jet, the estimate of the balanced contribution from surface density is not accurate in order to identify the internal tide signature. Inspection of the squared coherence between $\eta_{\text{tide},\rho}$ and $\eta - \bar{\eta}$ (blue curve in Figure 8, bottom right) shows that the proposed method correctly picks up the signature of the internal tide around the 180 km wavelength (left-most vertical black dashed line). The squared coherence between $\eta_{\text{tide},\rho}$ and $\eta - \bar{\eta}$ exhibits three maxima that correspond approximately to the wavelengths of mode 1 and mode 2 internal waves at frequency ω (black vertical dashed line) as well as mode 1 internal waves at frequency 2ω (grey vertical dashed line). The 2ω maximum translate, as expected, into local minima of the squared coherence between η_{tide} and $\eta - \bar{\eta}$ and that between η_{tide} and $\eta_{\text{tide},\rho}$ (orange and purple curves, respectively, in Figure 8, bottom right). Fast small scale motions that exhibit a signature on η but not on $\bar{\eta}$ nor on η_{tide} may explain the maximum found at high wavenumber.

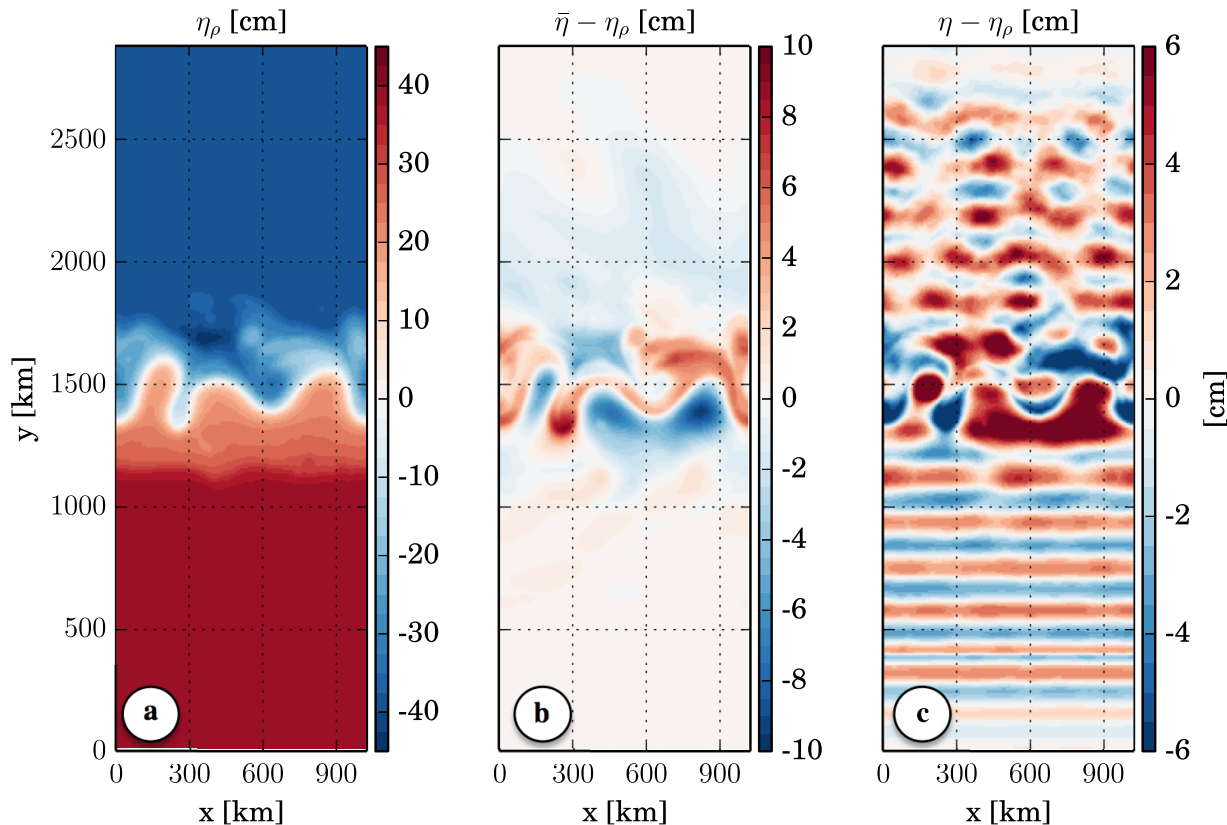


Figure 7. (a) Sea level estimated via PV inversion with PV estimated from surface density (η_ρ). (b) Difference between the 1 day averaged sea level ($\bar{\eta}$) and that obtained from the surface density via PV inversion (η_ρ). (c) Difference between instantaneous sea level (η) and that obtained from the surface density via PV inversion. Note that colors are saturated on the right as maximum values reach 9 cm.

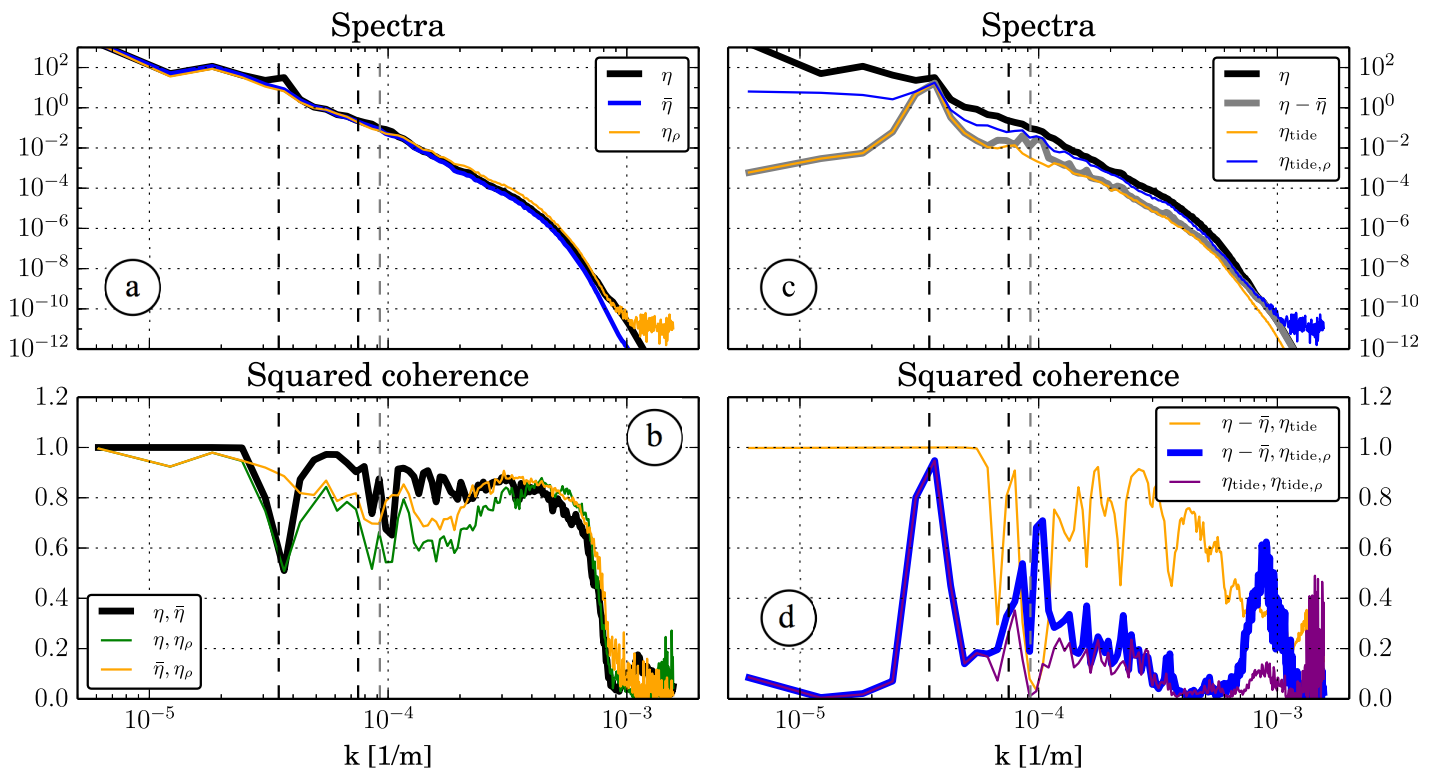


Figure 8. (a) Spectra of instantaneous sea level (black), averaged sea level (blue), reconstructed sea level (orange), $\bar{\eta}$ and η_ρ (orange). (b) Squared coherence between η and $\bar{\eta}$ (black), η and η_ρ (green), $\bar{\eta}$ and η_ρ (orange). (c) Spectra of instantaneous sea level (black), instantaneous minus 1 day averaged sea level (grey), tidal sea level (orange), instantaneous SSH minus that estimated from surface density via PV inversion (blue). (d) Squared coherence between $\eta - \bar{\eta}$ and η_{tide} (orange), between $\eta - \bar{\eta}$ and $\eta_{\text{tide},\rho}$ (blue), and, between η_{tide} and $\eta_{\text{tide},\rho}$ (purple). Vertical dashed lines corresponds to mode 1 and mode 2 tidal wavelengths (180 and 84 km, respectively), the grey dashed line corresponds to the mode 1 internal wavelength of frequency 2ω (68 km).

6. Discussion and Perspectives

Starting from snapshots of sea level and surface density, a method was proposed in order to achieve the ambitious task of distinguishing internal tide and balanced contributions. The cornerstone of the method lies in the weak signature of the low-mode internal tide on sea surface density and the correlation between sea surface density and interior potential vorticity anomalies. Sea surface density thus provides via potential vorticity inversion an estimate of the balanced stream function and hence sea level. Away from the turbulent jet, the method correctly identifies sea level fluctuations as being associated with the internal wave, which we consider a promising result. Near the turbulent jet, the estimate of balanced sea level from surface density is not accurate enough in order to discriminate tidal and balanced contributions. In such areas, the potential vorticity framework is nonetheless expected to remain useful as it provides information about the ocean balanced three-dimensional circulation [Lapeyre and Klein, 2006]. The method proposed here could already be tested with existing satellite observations of surface temperature in areas where the internal tide is sufficiently coherent that it can be extracted from altimetric data [Ray and Zaron, 2016].

The efficiency of the disentanglement is expected to decrease with increasing ratio of balanced to internal wave amplitudes as measured by their signature on sea level. Fortunately these situations where this ratio is high are also those where raw sea level is mostly representative of the balanced signal and the disentanglement of balanced and internal wave signals is least necessary. A promising perspective would be to feed the method with a priori statistical information about the relative magnitudes of these signals in observable variables in order to tie the treatment of these different situations. This could be achieved by minimizing a cost function that simultaneously accounts for potential vorticity constraints, expected signal strengths, as well as other dynamical constraints on the unbalanced signal (expected wavelengths for example).

Semidiurnal internal gravity waves have been considered here on the basis that this is representative of the strongest internal wave signatures on sea level. Wind-driven near-inertial waves indeed produce little sea level fluctuations naturally. As for higher frequency internal waves, these will be characterized by smaller

wavelengths at equal vertical structure. At equal wave signature on sea level, the method should thus better identify the internal wave signal at higher frequencies because of the red nature of the balanced flow wavenumber spectrum and the resulting larger relative amplitude of the internal wave fluctuations. Note, however, that the strength of internal waves also decreases with frequency in the ocean which may complicate the use of the present approach [Garrett and Munk, 1972, 1975; Polzin and Lvov, 2011].

In order to distinguish balanced and unbalanced contributions, the method strongly relies on its ability to reconstruct the three-dimensional distribution of potential vorticity from a sea surface variable observable from space that is not sea level. We found that surface density could lead to such reconstruction in an idealized numerical simulation of a turbulent meandering jet. The method will fail whenever the link between interior potential vorticity and surface density is nonexistent. This would, for example, happen in experiments where a balanced turbulence is driven at depth by a Phillips type instability with no signature on surface density [Ponte and Klein, 2013]. So, quid of the “real” Ocean? LaCasce and Mahadevan [2006] emphasizes that the estimation of interior potential vorticity from surface variables remains a difficult challenge. Lapeyre [2009] reports on the other hand that some correlation exists between potential vorticity and buoyancy below the mixed layer in a realistic numerical simulation of the North Atlantic. The correlation between remotely sensed sea level and surface temperature [Jones et al., 1998; Isern-Fontanet et al., 2006; Tandeo et al., 2014; Autret, 2014] or salinity [Reul et al., 2014] anomalies are indirect evidences that this link between interior dynamics and surface tracers occurs in energetic and frontal areas of the ocean. Due to instruments resolutions, these studies focused on the longer mesoscales though and one would have to examine whether this is the case at internal tide wavelengths (<200 km). One major obstacle is that surface tracers (e.g., temperature and salinity) are sensitive to air sea fluxes and to mixed layer dynamics. Surface mixed layers constitute a buffer which may obscure the relationship between observable surface variables and interior potential vorticity anomalies. Isern-Fontanet et al. [2008] and Wang et al. [2013] find for example that deeper mixed layer led to improved estimates of the interior ocean dynamics. Mixed layers may also complicate the estimation of the density required for the surface boundary condition of the potential vorticity inversion. The more appropriate density for the inversion is that at the bottom of the mixed layer which may not easily be estimated from remotely sensed variables. Compensation between surface temperature and salinity fluctuations may also complicate the estimation of density required for the surface boundary condition as it may require to combine both satellite observations of temperature and salinity [Stommel, 1993; Chen, 1995; Ferrari and Rudnick, 2000; Cole et al., 2010; Kolodziejczyk et al., 2015]. It unclear however whether such compensation will affect negatively or positively the estimation of interior potential vorticity. Overall much remains to be achieved in terms of testing the underlying assumptions and the applicability of the method proposed here in a realistic configuration. One way forward would be to increase the realism of the simulations presented here by adding a mixed layer dynamics and/or considering temperature and salinity dynamics. Realistic high resolution numerical simulations of the ocean circulation may also provide useful tools in order to proceed [Rocha et al., 2016]. At the moment, these simulations are actually the only way to verify that the regression coefficient ($\alpha(z)$) between the surface variable used to infer potential vorticity can be indeed estimated from large-scale fields (see (11) and Figure 6) which is critical to the practical implementation of the proposed method.

This work assumed the availability of simultaneous snapshots of sea level and sea surface density. In practice, these snapshots may not be synchronous which may introduce an additional difficulty. Multiple snapshots of these variables may turn out to help in the estimation of interior potential vorticity anomalies via data assimilation in balanced models [Ubelmann et al., 2015, 2016]. Spatial observations can fortunately be complemented with in situ data such as Argo at large scales (>300 km) in the upper half of the water column. This in situ data provide information about the large-scale potential vorticity gradients which, in our simulation as well as in a realistic configuration [Lapeyre, 2009], link surface density and interior via $\alpha(z)$ (see (11) and Figure 6). Such data also contain the signature of the fine scale ocean dynamics which could also be leveraged. Finally, while moving to finer scales or more energetic areas, larger Rossby numbers may require balance models of higher order [Penven et al., 2014].

Despite these potential roadblocks, this work was designed to advocate the use of the potential vorticity and more generally that of balance dynamics framework for the interpretation of high resolution ocean observations such as SWOT. These methods leverage the dynamical properties of the ocean circulation in order to draw direct links between such observations of the ocean three-dimensional dynamics and are to

Table A1. Root Mean Square (rms) Difference Between Instantaneous Sea Level η_i and the Sea Level Reconstructed by PV Inversion Under Various Boundary Conditions and Potential Vorticities^a

$z = 0$	$\partial_z \psi = -\frac{g\bar{\rho}}{\rho_0 f_0}$	$\partial_z \psi = -\frac{g\rho_i}{\rho_0 f_0}$			
q	\bar{q}	\bar{q}	\bar{q}	$\alpha(z)\rho_i$	$\alpha(z)\rho_i$
$z = -H$	$\partial_z \psi = -g\bar{\rho} / \rho_0 f_0$	$\partial_z \psi = -g\bar{\rho} / \rho_0 f_0$	$\psi = 0$	$\psi = 0$	$\partial_z \psi = -g\bar{\rho} / \rho_0 f_0$
rms ($\eta_i - \eta_\rho$)	1.853 cm	1.882 cm	2.087 cm	2.475 cm	4.939 cm

^aFor reference, the rms between η_i and $\bar{\eta}$ is 1.847 cm and that between η_i and $\bar{\eta} + \eta_{\text{tide}}$ is 0.173 cm.

our opinion a complementary approach to more costly direct assimilation approaches of the full ocean circulation.

Appendix A: Relative Importance of Surface Boundary Conditions and Potential Vorticity Approximations

A variance reduction experiment was carried on η_i in order to quantify the relative importance of boundary conditions and potential vorticity approximation on the decomposition of η_i into balanced and internal wave parts (Table A1). The root mean square difference (rms) between instantaneous sea level η_i and the sea level obtained after inversion η_ρ is to be compared with the rms difference between η_i and 1 day averaged sea level $\bar{\eta}$ which amounts to 1.847 cm and that between η_i and $\bar{\eta} + \eta_{\text{tide}}$ which amounts to 0.173 cm. The experiment indicates that the signature of internal waves on instantaneous density at the surface weakly affects the result of the inversion (first two columns). The potential vorticity approximation from sea surface density is responsible for most of the inaccuracy of the disentanglement. The assumption of no flow at the bottom (third column) does also contribute to the error. Finally, the combination of a bottom boundary condition based on density and an approximated potential vorticity leads to a very poor estimate of the tidal sea level (last column).

Acknowledgments

We acknowledge the support of IFREMER, CNRS, the Agence Nationale pour la Recherche [ANR-10-LABX-19-01 (LabexMER)], the CNES's SWOT mission, and the PRACE Research Infrastructure through allocation 2014102346. The data analyzed were obtained via numerical simulations whose set up is thoroughly described in the manuscript and the supporting information document.

References

- Arbic, B. K., F. Lyard, A. Ponte, R. Ray, J. G. Richman, J. F. Shriver, E. Zaron, and Z. Zhao (2015), Tides and the SWOT mission: Transition from science definition team to science team, Tech. rep., CNES-NASA. [Available at <https://swot.jpl.nasa.gov/science/resources/>]
- Autret, E. (2014), Analyse de champs de température de surface de la mer à partir d'observations satellite multi-sources, PhD thesis, Université Européenne de Bretagne, Brest.
- Chen, L. G. (1995), Mixed layer density ratio from the levitus data, *J. Phys. Oceanogr.*, 25, 691–701.
- Cole, S. T., D. L. Rudnick, and J. A. Colosi (2010), Seasonal evolution of upper-ocean horizontal structure and the remnant mixed layer, *J. Geophys. Res.*, 115, C04012, doi:10.1029/2009JC005654.
- Dufau, C., G. Dibarboue, M. Orszynowicz, R. Morrow, P.-Y. L. Traou, and N. Steunou (2014), (sub)mesoscale detection capability with along-track altimeter data, in *Ocean Surface Topography Science Team, Lake Constance*. [Available at <http://meetings.aviso.altimetry.fr/programs/complete-program.html>]
- Dunphy, M., and K. G. Lamb (2014), Focusing and vertical mode scattering of the first mode internal tide by mesoscale eddy interaction, *J. Geophys. Res. Oceans*, 119, 523–536, doi:10.1002/2013JC009293.
- Dunphy, M., A. L. Ponte, P. Klein, and S. L. Gentil, Low-mode internal propagation in a turbulent eddy field, *J. Phys. Oceanogr.*, in press. [Available at <http://journals.ametsoc.org/toc/phoc/0/0>]
- Ferrari, R., and D. L. Rudnick (2000), Thermohaline variability in the upper ocean, *J. Geophys. Res.*, 105(C7), 16,857–16,883.
- Fu, L.-L., D. B. Chelton, P.-Y. L. Traou, and R. Morrow (2010), Eddy dynamics from satellite altimetry, *Oceanography*, 23(4), 14–25, doi:10.5670/oceanog.2010.02.
- Garrett, C., and W. Munk (1972), Space-time scales of internal waves, *Geophys. Astrophys. Fluid Dyn.*, 3(1), 225–264.
- Garrett, C., and W. Munk (1975), Space-time scales of internal waves: A progress report, *J. Geophys. Res.*, 80(3), 291–297.
- Gill, A. E., and A. J. Clarke (1974), Wind-induced upwelling, coastal currents and sea-level changes, *Deep Sea Res. Oceanogr. Abstr.*, 21, 325–345.
- Griffies, S. M., et al. (2015), Impacts on ocean heat from transient mesoscale eddies in a hierarchy of climate models, *J. Clim.*, 28(3), 952–977.
- Hoskins, B. J., M. E. McIntyre, and A. W. Robertson (1985), On the use and significance of isentropic potential vorticity maps, *Q. J. R. Meteorol. Soc.*, 111(470), 877–946.
- Isern-Fontanet, J., B. Chapron, G. Lapeyre, and P. Klein (2006), Potential use of microwave sea surface temperatures for the estimation of ocean currents, *Geophys. Res. Lett.*, 33, L24608, doi:10.1029/2006GL027801.
- Isern-Fontanet, J., G. Lapeyre, P. Klein, B. Chapron, and M. W. Hecht (2008), Three-dimensional reconstruction of oceanic mesoscale currents from surface information, *J. Geophys. Res.*, 113, C09005, doi:10.1029/2007JC004692.
- Jones, M. S., M. Allen, T. Guymer, and M. Saunders (1998), Correlations between altimetric sea surface height and radiometric sea surface temperature in the South Atlantic, *J. Geophys. Res.*, 103(C4), 8073–8087.
- Klein, P., et al. (2015), Mesoscale/submesoscale dynamics in the upper ocean, Tech. rep., CNES-NASA. [Available at <https://swot.jpl.nasa.gov/science/resources/>]
- Kołodziejczyk, N., O. Hernandez, J. Boutin, and G. Reverdin (2015), SMOS salinity in the subtropical north Atlantic salinity maximum: 2. Two-dimensional horizontal thermohaline variability, *J. Geophys. Res. Oceans*, 120, 972–987, doi:10.1002/2014JC010103.

- LaCasce, J. H., and A. Mahadevan (2006), Estimating subsurface horizontal and vertical velocities from sea-surface temperature, *J. Mar. Res.*, *64*, 695–721.
- Lapeyre, G. (2009), What vertical mode does the altimeter reflect? On the decomposition in baroclinic modes and on a surface-trapped mode, *J. Phys. Oceanogr.*, *39*, 2857–2874.
- Lapeyre, G., and P. Klein (2006), Dynamics of the upper oceanic layers in terms of surface quasigeostrophy theory, *J. Phys. Oceanogr.*, *36*, 165–176.
- Le Traon, P. Y. (2013), From satellite altimetry to Argo and operational oceanography: Three revolutions in oceanography, *Ocean Sci.*, *9*, 901–915, doi:10.5194/os-9-901-2013.
- Penven, P., I. Halo, S. Pous, and L. Marié (2014), Cyclogeostrophic balance in the mozambique channel, *J. Geophys. Res. Oceans*, *119*, 1054–1067, doi:10.1002/2013JC009528.
- Polzin, K. L., and Y. V. Lvov (2011), Toward regional characterizations of the oceanic internal wavefield, *Rev. Geophys.*, *49*, RG4003, doi:10.1029/2010RG000329.
- Ponte, A. L., and P. Klein (2013), Reconstruction of the upper ocean 3D dynamics from high resolution sea surface height, *Ocean Dyn.*, *63*(7), 777–791, doi:10.1007/s10236-013-0611-7.
- Ponte, A. L., and P. Klein (2015), Incoherent signature of internal tides on sea level in idealized numerical simulations, *Geophys. Res. Lett.*, *42*, 1520–1526, doi:10.1002/2014GL062583.
- Ray, R. D., and G. T. Mitchum (1996), Surface manifestation of internal tides generated near Hawaii, *Geophys. Res. Lett.*, *23*, 2101–2104.
- Ray, R. D., and E. D. Zaron (2011), Non-stationary internal tides observed with satellite altimetry, *Geophys. Res. Lett.*, *38*, L17609, doi:10.1029/2011GL048617.
- Ray, R. D., and E. D. Zaron (2016), M_2 internal tides and their observed wavenumber spectra from satellite altimetry, *J. Phys. Oceanogr.*, *46*, 3–22.
- Reul, N., B. Chapron, T. Lee, C. Donlon, J. Boutin, and G. Alory (2014), Sea surface salinity structure of the meandering Gulf Stream revealed by SMOS sensor, *Geophys. Res. Lett.*, *41*, 3141–3148, doi:10.1002/2014GL059215.
- Richman, J. G., B. K. Arbic, J. F. Shriver, and E. J. Metzger (2012), Inferring dynamics from the wavenumber spectra of an eddy global ocean model with embedded tides, *J. Geophys. Res.*, *117*, C12012, doi:10.1029/2012JC008364.
- Rocha, C. B., S. T. Gille, T. K. Chereskin, and D. Menemenlis (2016), Seasonality of submesoscale dynamics in the kuroshio extension, *Geophys. Res. Lett.*, *43*, 11,304–11,311, doi:10.1002/2016GL071349.
- Roulet, G., J. C. McWilliams, X. Capet, and M. J. Molemaker (2012), Properties of steady geostrophic turbulence with isopycnal outcropping, *J. Phys. Oceanogr.*, *42*, 18–38.
- Shchepetkin, A. F., and J. C. McWilliams (2005), The regional ocean modeling system: A split-explicit, free-surface, topography-following coordinates ocean model, *Ocean Modell.*, *9*, 347–404.
- Shriver, J. F., J. G. Richman, and B. K. Arbic (2014), How stationary are the internal tides in a high-resolution global ocean circulation model?, *J. Geophys. Res. Oceans*, *119*, 2769–2787, doi:10.1002/2013JC009423.
- Stammer, D., et al. (2014), Accuracy assessment of global barotropic ocean tide models, *Rev. Geophys.*, *52*, 243–282, doi:10.1002/2014RG000450.
- Stommel, H. M. (1993), A conjectural regulating mechanism for determining the thermohaline structure of the oceanic mixed layer, *J. Phys. Oceanogr.*, *23*, 142–148.
- Tandeo, P., B. Chapron, B. Sileye, E. Autret, and R. Fablet (2014), Segmentation of mesoscale ocean surface dynamics using satellite SST and SSH observations, *IEEE Trans. Geosci. Remote Sens.*, *52*(7), 4227–4235.
- Ubelmann, C., P. Klein, and L.-L. Fu (2015), Dynamic interpolation of sea surface height and potential applications for future high-resolution altimetry mapping, *J. Atmos. Oceanic Technol.*, *32*, 177–184.
- Ubelmann, C., B. Cornuelle, and L. Fu (2016), Dynamic mapping of along-track ocean altimetry: Method and performance from observing system simulation experiments, *J. Phys. Oceanogr.*, *33*, 1691–1699.
- Vallis, G. K. (2006), *Atmospheric and Oceanic Fluid Dynamics*, Cambridge Univ. Press, Cambridge, U. K.
- Wang, J., G. R. Flierl, J. H. LaCasce, J. L. McClean, and A. Mahadevan (2013), Reconstructing the ocean's interior from surface data, *J. Phys. Oceanogr.*, *43*, 1611–1626.
- Zaron, E. D. (2015), Non-stationary internal tides observed using dual-satellite altimetry, *J. Phys. Oceanogr.*, *45*, 2239–2246.
- Zilberman, N., D. Roemmich, and S. Gille (2014), Meridional volume transport in the south pacific: Mean and SAM-related variability, *J. Geophys. Res. Oceans*, *119*, 2658–2678, doi:10.1002/2013JC009688.